Oxygen partial pressures on gas-diffusion layer surface and gas-flow channel wall in polymer electrolyte fuel cell during power generation studied by visualization technique combined with numerical simulation

Yuta Ishigami [a], Wihatmoko Waskitoaji [b], Masakazu Yoneda [c], Kenji Takada [a], Tsuyoshi Hyakutake [b], Takeo Suga [b], Makoto Uchida [d], Yuzo Nagumo [e], Junji Inukai [d, *], Hiroyuki Nishide [b, 1], Masahiro Watanabe [d, 2]

[a] Interdisciplinary Graduate School of Medicine and Engineering, University of Yamanashi, 4-3 Takeda, Kofu, Yamanashi 400-8511, Japan
[b] Department of Applied Chemistry, Waseda University, 3-4-1 Okubo, Shinjuku, Tokyo 169-8555, Japan
[c] Mizuho Information and Research Institute, Inc., 2-3 Kandanishiki-cho, Chiyodaku, Tokyo 101-8443, Japan
[d] Fuel Cell Nanomaterials Center, University of Yamanashi, 6-43 Miyamae-cho, Kofu, Yamanashi 400-0021, Japan
[e] Shimadzu, 3-9-4 Hikaridai, Seika-cho, Kyoto 619-0237, Japan

HIGHLIGHTS

- $p(O_2)$ was visualized at the GDL and the upper channel wall of a running PEFC.
- Two different oxygen-sensitive luminescent dye films were used.
- Different distributions of $p(O_2)$ were seen at the two locations inside a PEFC.
- A numerical calculation was carried out to understand the reactions inside the MEA.
- Water distribution influenced the current density and $p(O_2)$ in the MEA.

GRAPHICAL ABSTRACT
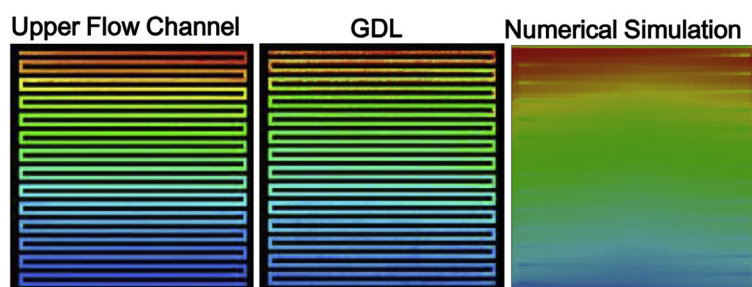
ARTICLE INFO

ABSTRACT

Visualization of the oxygen partial pressures was carried out at the surface of a gas diffusion layer (GDL) for the first time together with the upper part of the gas-flow channel of the cathode of a running polymer electrolyte fuel cell (PEFC) using two different oxygen-sensitive luminescent dye films. The visualized distributions of the oxygen partial pressures at the GDL and the upper gas-flow channel during the PEFC operation were very different in a conventional test cell. The change in the distribution of the oxygen partial pressures was observed by changing the oxygen utilization, which should be connected with the reactive locations in the membrane-electrode assembly (MEA). A numerical calculation was carried out to understand the distributions of water and current density inside the MEA. The water

---

* Corresponding author. Tel./fax: +81 55 254 7129.
  E-mail addresses: jinukai@yamanashi.ac.jp (J. Inukai), nishide@waseda.jp (H. Nishide), m-watanabe@yamanashi.ac.jp (M. Watanabe).
 [1] Tel.: +81 3 3200 2669; fax: +81 3 3209 5522.
 [2] Tel./fax: +81 55 254 7091.

Gas diffusion layer
Gas-flow channel
Oxygen reduction reaction
Numerical modeling

distribution inside the MEA was confirmed to strongly affect the distributions of the current density and the oxygen /partial pressure.
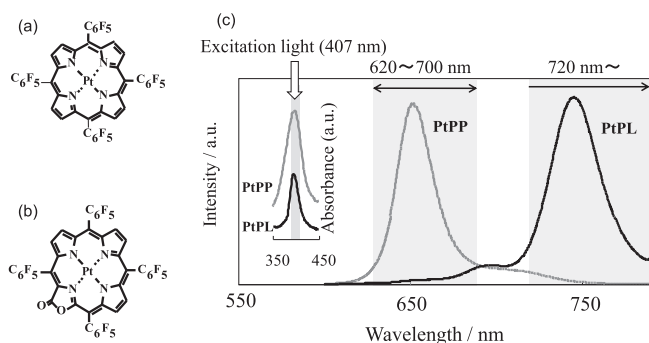
1. Introduction

Polymer electrolyte fuel cell (PEFC) is a new energy source expected to be widely used with its high power density and cleanliness. Although PEFCs have many advantages compared with current internal-combustion engines, the cost reduction and the improvement of durability/reliability are still needed. The development of new materials for the cell components and suitable cell designs are required. Adequate operation modes also need to be researched. For the improvement of PEFCs via the issues pointed out above, it is important to reveal the distribution of chemical species (O_2, H_2, H_2O, CO_2, H_2O_2, etc.) and physical parameters (temperature, current density, etc.) in a PEFC under the operating conditions and to feedback the so-obtained data into the designs of the membrane electrode assembly (MEA) and the PEFC itself. The visualization inside the PEFC, therefore, is essential.

Recently, visualization studies inside PEFCs have been focused mainly on liquid water to understand the flooding and plugging, which could occur in the catalyst layer, gas diffusion layer (GDL), and gas-flow channels to block supply gases. The water visualizations have been carried out by using various technologies: direct optical visualization [1–6], neutron radiography imaging [7–14], X-ray imaging [15–18], and magnetic resonance imaging (MRI) [19–21]. Those studies revealed that the generated water plays a key role in the performance and stability of the PEFCs. Now, the visualization of other chemical species, such as oxygen, is expected.

Our research group has developed a nondestructive, real-time/ space visualization system for oxygen partial pressure ($p(O_2)$) at the cathode of PEFCs [5,6,22–24] and a direct methanol fuel cell (DMFC) [25] under the operating conditions using a chemical probe for $p(O_2)$, "platinum-tetrakis(pentafluorophenyl)porphyrine (PtPP)" (Fig. 1(a)) [26]. In the previous papers, $p(O_2)$ was visualized only on the upper channel walls. In this paper, the distributions of $p(O_2)$ at the GDL surfaces, together with that on the upper channel walls, at the cathode were visualized for the first time using two different dyes: regularly-used PtPP and a new probe "platinum-tetrakis(pentafluorophenyl)porpholactone (PtPL)" (Fig. 1(b)) [27,28]. Experimentally, by using those dyes, different $p(O_2)$ distributions were visualized between at the GDL surface and at the upper position of a gas-flow channel.

For understanding the oxygen reduction reaction (ORR) in the MEA, or the reaction current distribution, we also carried out numerical and simulation inside the PEFC. To evaluate the performance of PEFCs speedily and accurately, our research group has developed a simulation tool including the macroscopic parameters of gas and heat transport in flow field and MEA characteristics such as electrochemical kinetics in the catalyst layer and proton/water transport in the electrolyte membrane [29]. In this paper, experimental and simulation data are carefully compared to demonstrate a new evaluation strategy for understanding the reaction distributions inside a PEFC. The simulation results gave clear explanations for the change of the $p(O_2)$ distributions under different cell-operation conditions.
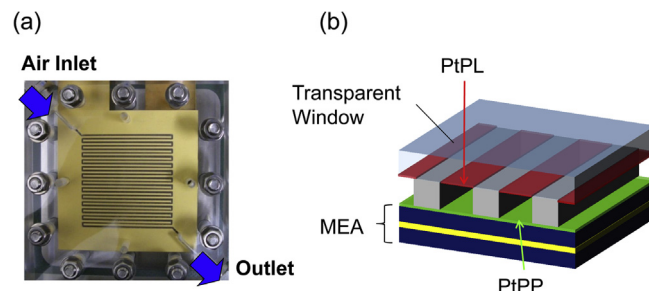
2. Experimental

2.1. Oxygen sensitive dye films and see-through PEFC

Toluene solutions of PtPP (Fig. 1(a)) and PtPL (Fig. 1(b)) were mixed with an oxygen-permeable polymer, poly(1-trimethylsilyl-1-propyne) (PMSP) at room temperature as previously reported [27,28]. Absorption and emission spectra of PtPP and PtPL are shown in Fig. 1(c). Both PtPP and PtPL have the absorption peaks approximately at 400 nm, but have different emission peaks at 650 and 750 nm, respectively. Therefore, $p(O_2)$ at two positions inside a cell can be visualized by using a single light source (407 nm).

Commercial MEAs with the Pt loadings of 0.4 mg cm^{-2} both on the anode and the cathode were used. The catalyst area was 52 mm × 52 mm. For the electrolyte membrane with a thickness of 30 μm, perfluorosulfonic acid ionomers were employed. On a gas diffusion layer with a thickness of approximately 200 μm, a microporous layer (MPL) with a thickness of several micrometers was attached.

A see-through cell with a transparent window was used for visualizing $p(O_2)$ in the PEFC under the operating condition. The endplate of a "Standard Cell of Japan Automobile Research Institute (JARI standard cell)" [30], a commonly-used cell employed for the development of PEFCs, at the cathode side was replaced by an acrylic plate to visualize inside the cell (Fig. 2(a)) [24,31]. PtPL was sprayed on a perfluoroalkoxy (PFA) film (film thickness = 2 μm), and the film was inserted between the endplate and the current collecting ribs. In this way, $p(O_2)$ on the upper wall of the gas-flow channel was visualized. On the other hand, PtPP was sprayed uniformly on the GDL surface at the cathode with the average thickness of 4 μm. The

Fig. 1. (a) Chemical structure of platinum-tetrakis(pentafluorophenyl)porphyrine (PtPP). (b) Chemical structure of platinum-tetrakis(pentafluorophenyl)porpholactone (PtPL). (c) Absorption spectrum and luminescence spectra of PtPP and PtPL.

Fig. 2. (a) Photograph of a see-through cell. (b) Schematic drawing of a flow field with two dye films.

locations of the dye films are schematically illustrated in Fig. 2(b). The channel depth and width of the cell were both 1 mm, therefore, the distance between the PtPP and PtPL films was also 1 mm.

2.2. Optical settings for the visualization of p(O₂)

The optical setting for visualization of $p(O_2)$ was essentially the same as that reported in previous papers [5,22,24,25]. Fig. 3 shows a schematic drawing of the optical system. A diode laser was used as a 407-nm light source, and the excitation light was diffused by diffuser plates and distributed uniformly onto the see-through cell. The emission lights from PtPP at the GDL surface and PtPL at the upper channel wall passed through an acrylic endplate and were separated by a hot mirror. Then, the lights were separately captured with two CCD cameras (500 × 500 pixels, 1 pixel = 100 × 100 μm) in a dark room. CCD camera 1 in Fig. 3 with a band-pass filter (620 < λ < 700 nm) in front was used for detecting $p_{(O_2)}$ on the GDL surface, whereas CCD camera 2 with a cutting filter (λ > 720 nm) for detecting $p_{(O_2)}$ on the upper channel wall. In this way, the images on the GDL and on the upper wall of the gas-flow channel were separately and simultaneously obtained.

2.3. Visualization of p(O₂)

Prior to the power generation, the calibration curves, known as Stern−Volmer plots, of PtPP and PtPL were obtained by the same way as reported previously [22,24,25] under the mixed gases of oxygen and nitrogen (oxygen concentration = 0−25%) at 80 °C supplied to both cathode and anode gas-flow channels at the gas-flow rate of 50 mL min⁻¹. The cell operation was performed at 80 °C, with the humidified air and hydrogen (60% RH) being supplied to the cathode and the anode, respectively, at 300 mL min⁻¹. Oxygen utilization(U_{O_2}) was set at 0, 20, 30, 60, and 80%. During the operation, the laser light was irradiated onto the cell, and the light emission from the GDL surface and the upper channel wall were separately captured by CCD cameras. The time and space resolutions were 250 ms and 100 μm, respectively. Under the steady state condition, 32 emission images were continuously captured to be averaged on the computer. Distributions of the emission were converted to the $p(O_2)$ images on the upper channel wall and on the GDL surface using the Stern−Volmer plots acquired previously for both dyes.

3. Numerical modeling

Inside PEFCs, multi-physical and multi-scale phenomena, such as gas/heat transports in the flow channel and the GDL with an MPL, electrochemical reactions, and proton/water transports in the
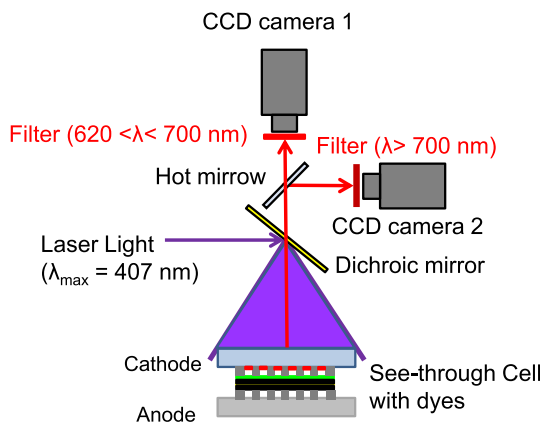
MEA, are nonlinearly coupled [32]. These phenomena require a large amount of efforts to solve many equations by fully three-dimensional fundamental equations based on Computational Fluid Dynamics (CFD), so it is necessary to apply simplified models and cut the calculation cost down. In this study, macroscopic models are applied for the phenomena inside the MEA, such as electrochemical reactions and proton/water transport. Furthermore, these models are coupled with multi-dimensional heat and mass-transport equations, in which effective parameters such as gas diffusivity and permeability in the GDL/MPL and the equivalent diameter of the flow channel are included. These parameters are emphasized with superscript "eff" in the following equations.

3.1. Models for mass and heat transport

In this study, the mass and heat transports in the flow field are modeled. Reynolds number in the cathode channel under the present experimental conditions was first calculated to confirm the laminar flow in the channel. In the flow channel, the one-dimensional gas, liquid water and heat transport equations, in which the pressure drop is assumed to be of the laminar flow, are applied. In the GDL with an MPL, the fully three-dimensional gas, liquid water, and heat transport equations with multi-component gas diffusion are applied, in which the pressure drop is assumed to follow the Darcy's law. The advantage of these simplified models for the flow calculation is a substantial reduction of calculation cost in comparison with CFD. Therefore, these models can simulate a large-scale cell performance in a short period (about half a day using a most recent personal computer). These equations are shown below.

- conservation equation of mass:

$$\begin{cases} \varepsilon\dfrac{\partial}{\partial t}\left[\rho_g(1-s)\right] + \nabla\cdot\left[\rho_g(1-s)\mathbf{u}_g\right] = \displaystyle\sum_k \dot{m}_{p,g}^k + \dot{m}_g^{H_2O} \\[4mm] \varepsilon\dfrac{\partial}{\partial t}(\rho_l s) + \nabla\cdot(\rho_l s\mathbf{u}_l) = -\dot{m}_g^{H_2O} \end{cases} \quad (1)$$

- equation of pressure loss in the flow field (based on Darcy's law):

$$\begin{cases} \mathbf{u}_g = -\dfrac{K}{\mu_g}(1-s)^{n_g}\nabla p \\[4mm] \mathbf{u}_l = -\dfrac{K}{\mu_l}s^{n_l}(\nabla p - \nabla p_c) \end{cases} \quad (2)$$

In the flow channel, the permeability, K, is replaced by the parameter with equivalent diameter, d_e, of a laminar pipe flow, and the capillary pressure, p_c, as a function of water saturation is assumed to be zero.

$$K = \frac{d_e^2}{32} \quad (3)$$

- conservation equation for chemical species:

$$\varepsilon\frac{\partial}{\partial t}\left[(1-s)c_g^k\right] + \nabla\cdot\left[c_g^k\mathbf{u}_g - c_g D_g^{k,\mathrm{eff}}\nabla\left(\frac{c_g^k}{c_g}\right)\right] = \dot{m}_{g,p}^k + \dot{m}_{gl}^{H_2O} \quad (4)$$

CCD camera 1

Filter (620 <λ< 700 nm)   Filter (λ> 700 nm)

Hot mirror

CCD camera 2

Laser Light
(λ_max = 407 nm)

Dichroic mirror

Cathode

Anode

See-through Cell
with dyes

Fig. 3. Schematic representation of the optical settings for the p_{O_2} visualization.

where $\dot{m}_{gl}^{H_2O}$ is the mass production by phase-change that is formulated as follows:

$$\dot{m}_{gl}^{H_2O} = -\omega_{gl} w^{H_2O} \left(c_g^{H_2O} - \frac{p_s}{RT} \right) \qquad (5)$$

- conservation equation of energy

$$(1-\varepsilon)\frac{\partial}{\partial t}\rho_s h_s + \varepsilon\frac{\partial}{\partial t}\left[\rho_g(1-s)h_g + \rho_l s h_l\right]$$
$$+ \nabla\cdot\left[\rho_g(1-s)h_g\mathbf{u}_g + \rho_l s h_l\mathbf{u}_l\right] = \nabla\cdot\left(\kappa^{eff}\nabla T\right) + \dot{q}_{(m)} \qquad (6)$$

3.2. Models for electrochemical reactions and for transports of protons and water

Electrochemical reactions and water transports in the MEA are treated with parametric models, which involve the partial pressure of reactants and the temperature at the closest mesh point to the MEA as representative parameters. Electrochemical reactions are assumed to follow the Butler–Volmer equation and occur at the interface between the MPL and the electrolyte membrane. The catalyst layer is treated as a planar surface.

$$i = i_{0(k)}\left[\exp\left(\frac{\alpha_{a(k)}^+ F}{RT_{(m)}}\eta_{a(k)}\right) - \exp\left(-\frac{\alpha_{a(k)}^- F}{RT_{(m)}}\eta_{a(k)}\right)\right] \qquad (7)$$

$$i_{0(k)} = i_{0(k),ref}\,\theta_{(k)}^{eff}\left(\frac{p_{(k)}}{p_{(k),ref}}\right)^{\gamma_{(k)}}\exp\left[-\frac{G_{(k)}}{R}\left(\frac{1}{T_{(m)}} - \frac{1}{T_{ref}}\right)\right] \qquad (8)$$

Here, $\theta_{(k)}^{eff}$ is catalyst utilization which depends on the MEA characteristics. Ohmic over-potential due to a proton transport in the electrolyte membrane is described by the following equations according to the model proposed by Nguyen and White [33].

$$\eta_r = i\frac{t_{(m)}}{\sigma_{(m)}^{eff}} \qquad (9)$$

$$\sigma_{(m)}^{eff} = \sigma\left(a_{(m)}^v\right)\exp\left[1268\left(\frac{1}{303} - \frac{1}{T_{(m)}}\right)\right] \qquad (10)$$

Each mass flux of the chemical species generated by the electrochemical reaction is given by the following expressions. As for the water transport through the electrolyte membrane, both the electro-osmotic drag and the water diffusion are considered.

- Mass flux by electrochemical reactions

$$\dot{m}_p^k = -w^k\frac{\partial}{\partial z}\left(\frac{i}{n^k F}\right) \qquad (11)$$

- Water transport flux

$$\dot{m}_p^{H_2O} = -w^{H_2O}\frac{\partial}{\partial z}\left(n_d^{eff}\frac{i}{F} - \frac{\rho_{(m)}^{dry}}{EW}D_w^{eff}\frac{\partial\lambda_{(m)}}{\partial z}\right) \qquad (12)$$

Heat production by the over-potential is calculated by the following equation.

$$q_{(m)} = \frac{i}{t_{(m)}}\left(\eta_{a(a)} + \eta_{a(c)} + \eta_r\right) \qquad (13)$$

For solving the continuum Equations 1–13 under the boundary conditions shown in Table 1, it is necessary to determine the macroscopic parameters. These parameters could be determined directly using the results of a micro-scale simulation, for example, molecular dynamics simulation in the catalyst layer and the electrolyte membrane and fully Navier–Stokes simulation in the flow field. In this study, however, they are adjusted to reproduce quantitatively the measured polarization curves of a small-sized cell and pressure drop in the flow channel under several conditions for different relative humidities, oxygen gas concentrations and cell temperatures. The reactant gas utilization is very low (less than 1%) in order to obtain the sufficient liquid water removal in the flow field and the uniform current distribution [29]. The final fitting parameters using in this study are shown in Table 2.

4. Results and discussion

Fig. 4(a) and (b) show the Stern–Volmer plots of PtPP and PtPL dye films, respectively, placed in a see-through cell. p_{ref} is the oxygen partial pressure and I_{ref} the emission intensity obtained in air. Both the Stern–Volmer plots of PtPP and PtPL appeared nearly linear. The plots were fit with cubic polynomials, which were used for the calibration curves. The performance of the see-through cell with PtPL and PtPP dyes coated inside was examined before the visualization. Fig. 5 shows the current density-voltage (I–V) curves obtained in a see-through cell with/without dye films. The I–V curve of a see-through cell without dyes (blue line) was approximately identical to that of a JARI standard cell. With a PtPL dye film on the upper channel wall (red line), the I–V curve overlapped with that without dyes. Additional coating of a PtPP dye film on the GDL surface slightly lowered the voltage at a high current density above 0.7 V, probably because of the smaller gas diffusivity at the GDL surface. Overall, the cell performance was high even with dye films.

Fig. 6 show the time-resolved visualization images of the distributions of $p(O_2)$ at the upper channel wall (Fig. 6(a)–(e)) and at the GDL surface (Fig. 6(f)–(j)) simultaneously obtained at the cathode during the cell operation. The color of the images corresponds to $p(O_2)$. Air was supplied from the upper left and was exhausted from the lower right. Fig. 6(a) and (f) show the steady-state $p_{(O_2)}$ at $U_{O_2} = 20\%$. Then, U_{O_2} was abruptly changed from 20% to 80%, and the data acquisition was carried out with a time resolution of 250 ms. At the upper channel wall at 0.25 s (Fig. 6(b)), in which the signals were accumulated between 0 and 0.25 s, no distinctive change was seen. However, on the GDL surface (Fig. 6(g)), the change in $p_{(O_2)}$ was clearly observed, showing the

Table 1
Boundary conditions.

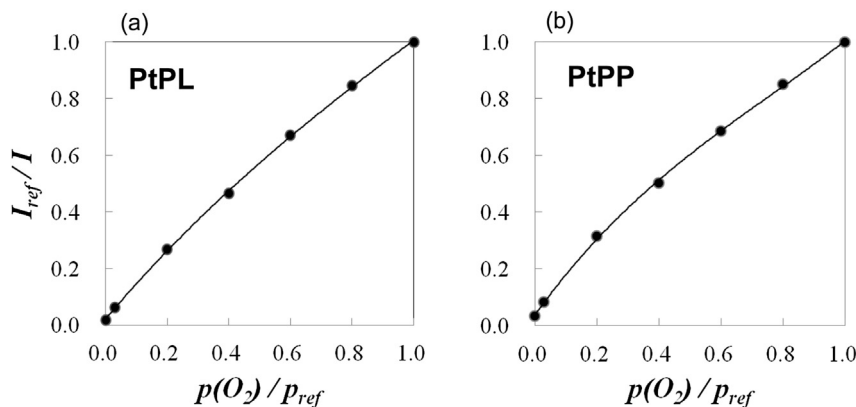| Parameters	Values
Anode inlet	Hydrogen: 300 mL min^{-1}
	Relative humidity: 60% RH
	Temperature: 353.15 K
Cathode inlet	Air: 300 mL min^{-1}
	Relative Humidity: 60% RH
	Temperature: 353.15 K
Anode/cathode outlet	Pressure: 101.325 kPa (abs)
Cell temperature	353.15 K (on the upper/lower boundary of a cell)

Table 2
Model parameters for MEA and GDL.

Parameters	Values
Butler–Volmer equation (electrochemical reaction)	$i_{0(a),ref} = 1.0 \times 10^{0}$ A cm^{-2} $\alpha^{\pm}_{(a)} = 0.25$, $\gamma_{(a)} = 0.5$ $i_{0(c),ref} = 1.0 \times 10^{-5}$ A cm^{-2} $\alpha^{\pm}_{(c)} = 1.35$, $\gamma_{(c)} = 0.9$
Catalyst utilization	$\theta_{(a)} = 1.0$, $\theta_{(c)} = a_{v(c)}$
Proton conductivity in the PEM	$\sigma^{eff}_{(m)} = 0.5\lambda_{(m)} - 0.326$
Osmotic-drag and water diffusivity	Springer et al. [34]
Porosity	$\varepsilon_{GDL} = 0.8$, $\varepsilon_{MPL} = 0.4$
Permeability	$K_{GDL} = 4.0 \times 10^{-12}$ m^2 $K_{MPL} = 1.0 \times 10^{-13}$ m^2
Effective diffusivity	$D^{eff}_i = D_i \cdot [\varepsilon(1-s)]^{2.5}$
Equivalent diameter of flow channel	$d_e = 1.0 \times 10^{-3}$ m
Phase change rate	$\omega_{gl} = 1.0 \times 10^{2}$ s^{-1}

Fig. 5. Current density–voltage curves in a see-thorough cell without dyes (blue line), with a PtPL film on the upper flow channel (red line), and with a PtPL film on the upper flow channel and PtPP on the GDL (green line). Cell temperature = 80 °C; relative humidity = 60% (air and H$_2$); a constant gas flow rate for hydrogen and air = 300 mL min^{-1}. (For interpretation of the references to color in this figure legend, the reader is referred to the web version of this article.)
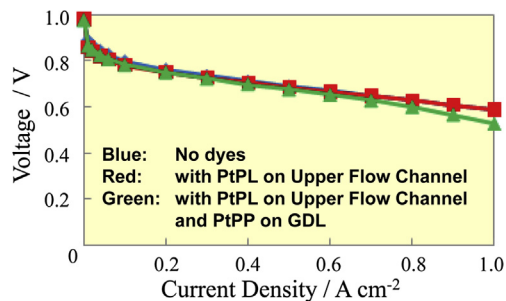
lowering of $p_{(O_2)}$ near the outlet. Notably, the decrease of $p_{(O_2)}$ was not along the channel length, but directly from the inlet to the outlet, as a contour line (dashed line) around 11 kPa shows. At 0.5 s, the change in $p_{(O_2)}$ became larger on the GDL surface (Fig. 6(h)), and on the upper channel wall, the change in $p_{(O_2)}$ also appeared. (Fig. 6(c)). On the upper flow channel, the influence of the cross flow was much smaller than that on the GDL; a contour line was rather parallel to the flow channel. After 1.0 s, the distributions of $p_{(O_2)}$ were still observed to be changing. It took several minutes before the $p_{(O_2)}$ images were apparently stabilized both on the GDL and the upper channel wall.

The steady-state distributions of p_{O_2} are presented in Fig. 7. The exposure time for each image was 8.0 s Fig. 7(a)–(d) shows the distributions of $p(O_2)$ at the upper channel wall, whereas Fig. 7(e)–(h) at the GDL surface at the cathode during the cell operation. The visualizations were carried out at $U_{O_2} = 0$, 30, 60 and 80%. In our previous papers, we have reported the visualization of liquid water in a DMFC [25] and on the GDL of a PEFC [6]. Even the simultaneous visualizations of $p(O_2)$ and liquid water have been carried out [5]. During the visualization of $p(O_2)$ in the present study in a single-serpentine cell, no liquid water was observed in the cathode gas-flow channel.

In the case of $U_{O_2} = 0\%$ (0 A cm^{-2}), although the cell was at the open circuit with no power generation, $p(O_2)$ at both the GDL surface and the upper gas-flow channel was seen to decrease uniformly from 15 to 14 kPa due to the total pressure loss along the gas-flow channel. When the cell was operated at $U_{O_2} = 30\%$ (0.22 A cm^{-2}), $p(O_2)$ uniformly decreased by the ORR along the gas-flow channel from the inlet to the outlet as seen in Fig. 7(b).

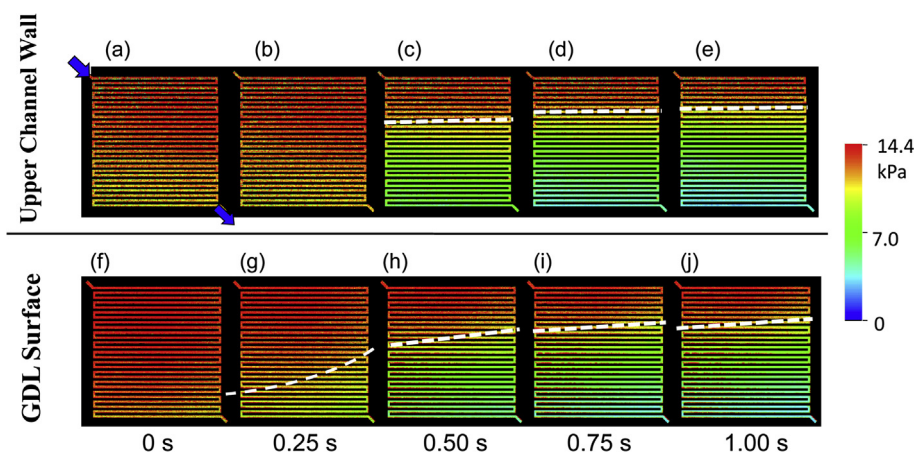However, $p(O_2)$ at the GDL surface was different; $p(O_2)$ significantly decreased in the middle of the gas-flow channel with a change of colors from red to green as seen in Fig. 7(f). Similarly, at $U_{O_2} = 60$ and 80%, the distribution of $p(O_2)$ at the upper channel wall was uniformly decreased, but the distributions of $p(O_2)$ at the GDL surface were not identical to those at the upper channel wall. The influence of the air flow through the GDL is clearly seen, which makes a $p(O_2)$ pattern on the right side on the GDL surface, for example, slightly higher than on the left side, notably observed in Fig. 7(f). For emphasizing the difference of $p(O_2)$ at the GDL surface and at the upper channel wall, $\Delta p(O_2) = (p(O_2)$ at upper channel wall) $- (p(O_2)$ at GDL) was calculated from Fig. 7 and plotted in Fig. 8. At $U_{O_2} = 0\%$, $\Delta p(O_2)$ was nearly equal to 0 kPa at any location as expected. At $U_{O_2} = 30\%$, $\Delta p(O_2)$ is larger in the latter half of the MEA. At $U_{O_2} = 60\%$, $\Delta p(O_2)$ is the largest in the upper middle area of the MEA, and at 80%, $\Delta p(O_2)$ is the largest at the upper location of the MEA. Therefore, the reactive area on the MEA is expected to differ at different reaction conditions.

To examine the data in more details, $p(O_2)$ measured at the upper channel wall and the GDL surface are plotted along the channel length. When U_{O_2} was 0% at the open-circuit voltage (Fig. 9), the average $p(O_2)$ value at the upper channel wall (red line) was the same as that at the GDL surface (blue line). $p(O_2)$ at the different locations decreased gradually from the inlet (15 kPa) to the outlet (14 kPa), because of a pressure loss. Periodic, sharp spikes were seen both on the upper channel wall and the GDL at the turns of the serpentine channel, but the spikes were much

Fig. 4. Stern–Volmer plots for PtPL (a) and PtPP (b) in the mixtures of oxygen and nitrogen. Cell temperature = 80 °C. The emission intensity, I, was measured for different oxygen partial pressures, $p(O_2)$. I_{ref} is the emission intensity at p_{ref}, the oxygen partial pressure in air.

Fig. 6. Time-resolved, simultaneous visualization of the oxygen partial pressures at the upper channel wall (a)–(e) and on the surface of GDL (f)–(j) in an operating PEFC. The oxygen utilization was changed from 20% to 80% at 0 s. Cell temperature = 80 °C; relative humidity = 60% (air and H$_2$); a constant gas flow rate for hydrogen and air = 300 mL min^{-1}. Time resolution was 250 ms. (For interpretation of the references to color in this figure legend, the reader is referred to the web version of this article.)

larger on the GDL. Those spikes at the turns will be later explained by the numerical simulation. At U$_{O_2}$ = 30, 60, and 80%, p(O$_2$) measured at the upper channel wall (Fig. 10(b)–(d)) and the GDL surface (Fig. 10(f)–(h)) are plotted with gray lines along the gas-flow channel length from the inlet to the outlet (1400 mm in length). At U$_{O_2}$ = 30%, p(O$_2$) at the upper channel wall gradually decreased from the inlet (15 kPa) to the outlet (10 kPa) (Fig. 10(b)), whereas p(O$_2$) on the GDL surface was clearly lower than that at the upper channel wall (Fig. 10(f)) at the latter half of channel (500–1400 mm). Periodic spikes were seen as in the case at U$_{O_2}$ = 0% (Fig. 9). The change in p(O$_2$) at the GDL in Fig. 10(f) is large in the middle of the length of the gas channel. From the point approximately at 500 mm to the outlet, p(O$_2$) at the GDL is always lower than that at the upper channel wall (Fig. 10(f)), showing that the oxygen might not be efficiently supplied to the GDL surface from the channel and that some part of air in the channel could be simply blown out at the upper part of the gas channel to the outlet due to the depth of the channel, 1 mm, and to a relatively high flow-rate of air (Fig. 2(b). At U$_{O_2}$ = 60%, p(O$_2$) at

the upper channel wall was gradually decreased from the inlet (15 kPa) to the outlet (5 kPa) (Fig. 10(c)), whereas p(O$_2$) at the GDL surface steeply lowered around 300–500 mm due to the increased ORR (Fig. 10(f)). In the case at the highest U$_{O_2}$ of 80%, p(O$_2$) at the GDL surface was drastically decreased near the inlet of the gas-flow channel around 200 mm (Fig. 10(h)). On the other hand, p(O$_2$) at the upper channel wall decreased smoothly from the inlet (15 kPa) to the outlet (2 kPa) (Fig. 10(d)). Comparing the results at U$_{O_2}$ = 30, 60, and 80% in Fig. 10, Δ p(O$_2$) was confirmed to move forward along the gas-flow channel (Fig. 8). At a low U$_{O_2}$ of 30%, the electrolyte membrane takes the water vapor formed at the upper air stream, which could mainly be accumulated at the lower part of the gas-flow channel via the GDL into the membrane and the catalyst layer. The proton conductivity of the electrolyte membrane thus should be improved, resulting in an enhanced ORR rate in this region. At a higher U$_{O_2}$ of 60%, a larger amount of water vapor was generated than at U$_{O_2}$ = 30% closer to the inlet, then the proton conductivity and the reaction might have increased at the middle part of the flow length. When U$_{O_2}$ = 80%,
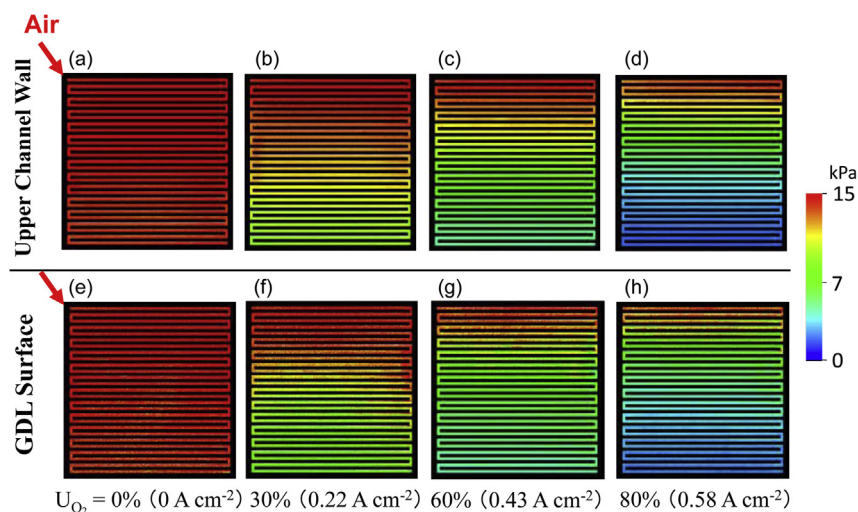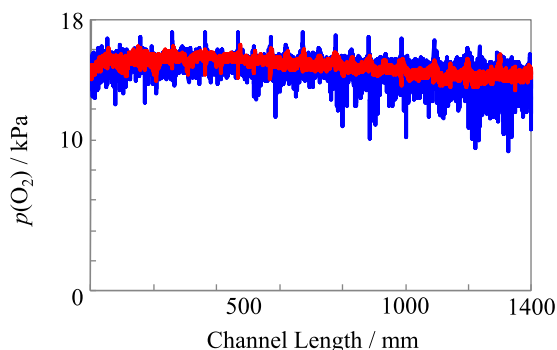

Fig. 7. Oxygen partial pressures at the upper channel wall (a)–(d) and on the surface of GDL (e)–(h) visualized experimentally in an operating PEFC. Cell temperature = 80 °C; relative humidity = 60% (air and H$_2$); a constant gas flow rate for hydrogen and air = 300 mL min^{-1}; oxygen utilization = 0 (a)(e), 30 (b)(f), 60 (c)(g), and 80% (d)(h), corresponding to overall current densities at 0, 0.22, 0.43 and 0.58 A cm^{-2}, respectively. 32 images were accumulated for each set of conditions.
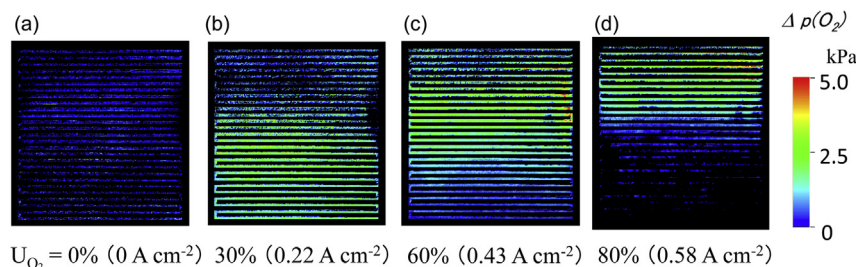
Fig. 8. $\Delta\,p(O_2)$ ($(p(O_2)$ at upper channel wall) $-$ $(p(O_2)$ at GDL)) calculated from Fig. 3. Cell temperature $= 80\ ^\circ C$; relative humidity $= 60\%$ (air and H_2); a constant gas flow rate for hydrogen and air $= 300\ mL\ min^{-1}$; oxygen utilization $= 0$ (a), 30 (b), 60 (c), and 80% (d). (For interpretation of the references to color in this figure legend, the reader is referred to the web version of this article.)

liquid water should exist in a wide range of the catalyst layer and the membrane, and the reaction rate should be the highest near the inlet with a decent amount of water. On the other hand, $p(O_2)$ at the upper flow-channel wall did not show a steep change because of less influence from the MEA. The difference in the $p(O_2)$ changes between these two layers is attributed partly to the non-optimized flow-channel design and could be reduced by increasing the gas flux, e.g., by reducing the rib height of the gas-flow channel even at the same U_{O_2} (in practical applications, the depth of the channels is normally less than 0.5 mm). The change of the channel design might result in a higher cell performance due to the smaller over-potential for the ORR by increasing the mass transfer.

In order to understand those processes more profoundly, a numerical simulation was carried out using a fuel-cell model described in Numerical Modeling section. Simulated $p(O_2)$ both at the upper channel wall and at the surface of GDL are plotted in dark along the gas-flow channel from the inlet to the outlet in Fig. 10 for the comparison with the experimental data shown in gray. The distributions of $p(O_2)$ were quantitatively in good agreement with experimental data at high U_{O_2}, especially at 80%, both on the upper channel wall and the GDL. On the other hand, at $U_{O_2} = 30\%$, the distribution of $p(O_2)$ was different from the experimental result, especially at the downstream area on the GDL (Fig. 10(f)). These results indicate that the oxygen consumptions by the ORR estimated at the numerical simulation does not correspond to the actual values at low U_{O_2}.
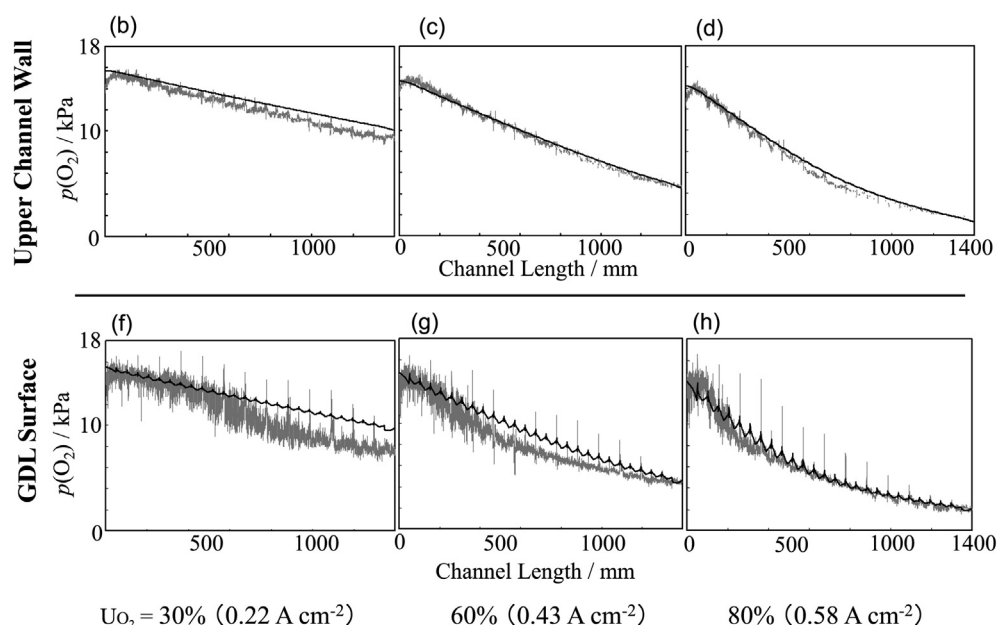

Fig. 9. Oxygen partial pressures at the open-circuit voltage at the upper channel wall (red line) and on the GDL surface (blue line) along the gas-flow channel length from the inlet (0 mm) to the outlet (1400 mm). Experimental data were obtained from the visualization data in Fig. 3. Cell temperature $= 80\ ^\circ C$; relative humidity $= 60\%$ (air and H_2); a constant gas flow rate for hydrogen and air $= 300\ mL\ min^{-1}$. (For interpretation of the references to color in this figure legend, the reader is referred to the web version of this article.)

The distributions $p(O_2)$ on the cathode catalyst layer, the local current density on the MEA, and the water vapor activity in the polymer electrolyte membrane derived from the numerical simulations are shown in Fig. 11(a)–(i), respectively, at different U_{O_2}, which can be compared to the experimental results shown in Fig. 7. For $p(O_2)$ (Fig. 11(a)–(c)) and the water vapor activity (Fig. 11(g)–(i)), the absolute partial pressures and the relative humidities are colored, respectively, whereas for the local current density, the color shows the difference from the average values in percent. At $U_{O_2} = 30\%$, $p(O_2)$ (Fig. 11(a)) decreased, and the current density (Fig. 11(d)) and the water activity (Fig. 11(g)) increased smoothly along the gas-flow channel from the inlet to the outlet. However, the $p(O_2)$ values experimentally visualized on the GDL (Fig. 7(f)) decreased significantly in the middle of the gas-flow channel (Fig. 10(f)) and deviated from those simulated (Fig. 11(a)), because of the large oxygen consumption. This discrepancy and insufficiency of the numerical model are probably caused by the insufficient estimation of the water vapor transport through the MEA, which directly affects the proton conductivity in the catalyst layer and the electrolyte membrane. According to the experimental results, the actual hydration inside the MEA under low relative humidity and low current density should be larger than that estimated by the simulation. Recently, we reported that the water distributions across the electrolyte membranes during the cell operation are very complex [35,36]. Therefore, the experimental data of the water distribution inside the membrane are essential to improve the numerical simulation. At $U_{O_2} = 60$ and 80%, the MEA should be much hydrated by produced liquid water (Fig. 11(h) and (i)) during the power generation (Fig. 11(e) and (f)), and the proton conductivity accordingly increased. Therefore, the effect of water vapor transport could be practically ignored. At higher U_{O_2}, the distributions of water activity in the MEA and thus $p(O_2)$ data were better simulated (Fig. 10(g) and (h)), and the peaks of current density were numerically reproduced to shift closer to the inlet as U_{O_2} increased (Fig. 11(e)–(f)). The oxygen consumption model at different U_{O_2} suggested by the experimental data are computationally supported.

In the experimental data of $p(O_2)$ in Figs. 8 and 10, especially in the data on the GDL, sharp spikes are seen both upwards and downwards. The positions of the spikes were well simulated; the spikes are observed at turns of a serpentine gas-flow channel. The sudden decrease and increase of $p(O_2)$ can be explained by the air flow through the GDL, short-cutting the flow channel. The intensity of the spikes is as large as several kilopascals, which should be large enough to have an influence on the cell performance.

In this paper, we visualized $p(O_2)$ on the GDL surface for the first time, and compared the data with those on the upper flow channel. By using our visualization method, we demonstrated a capability of providing better operating conditions during the power generations and keys to a design of better MEAs and flow fields of fuel cells. Numerical simulation was carried out for the visualization

Fig. 10. Oxygen partial pressures at the upper channel wall (b)–(d) and on the surface of the GDL (f)–(h) along the gas-flow channel length from the inlet (0 mm) to the outlet (1400 mm). Experimental and numerical calculation data are shown in gray and dark, respectively. Experimental data were obtained from the visualization data in Fig. 3. Oxygen utilization = 30 (b)(f), 60 (c)(g), and 80% (d)(h).

system. The comparison of experimental and simulation data was also confirmed to be useful in understanding the distributions of various physical and chemical properties inside the fuel cell. In order to improve the accuracy of the simulation, the water transport model used here must be improved. For this purpose, understanding the water distribution inside the membrane is essential, which is now in progress.

5. Conclusions

$p(O_2)$ at the GDL and the upper channel wall at the cathode of an operating PEFC was visualized, revealing the different distributions at different locations in the gas-flow channel. At low U_{O_2}, $p(O_2)$ on the upper channel wall gradually decreased along the length of the gas-flow channel, whereas that at the GDL was found to decrease
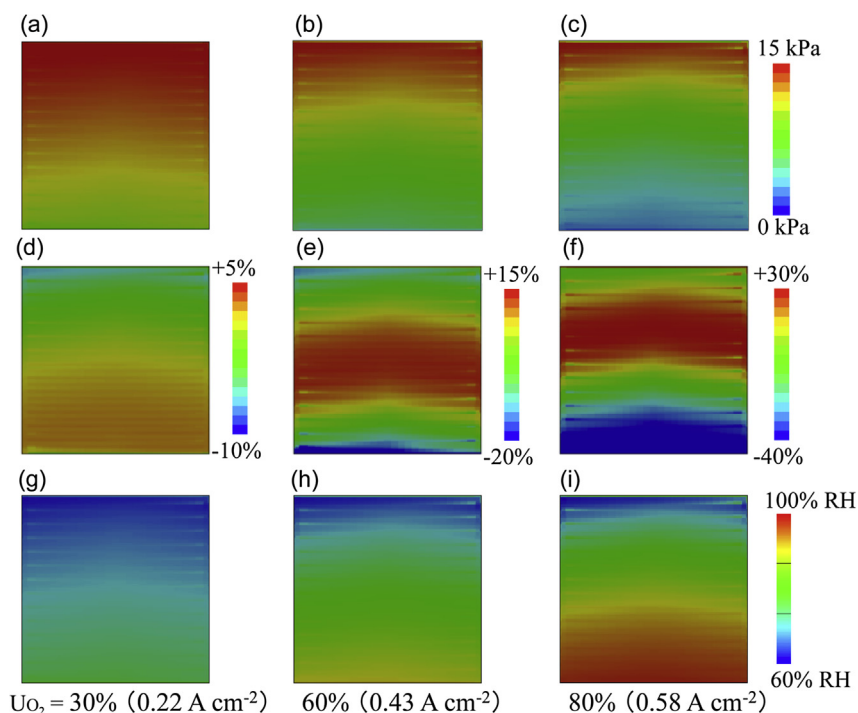
Fig. 11. Numerically-simulated distributions of $p(O_2)$ on the cathode catalyst layer (a)–(c), the local current density on the MEA (d)–(f), and the water vapor activity in the polymer electrolyte membrane (g)–(i). The cell operation conditions used for the simulation are the same as those shown in the captions of Fig. 3. (For interpretation of the references to color in this figure legend, the reader is referred to the web version of this article.)

significantly at the center of the length of the flow channel. By increasing U_{O_2}, the steep decrease in $p(O_2)$ at the GDL shifted closer to the inlet. The change in the distribution of $p(O_2)$ should be reflecting the reaction distribution in the MEA, which was supported by the numerical simulation. This dual visualization technique combined with the simulation is expected to be used for the cell and MEA designing.

Acknowledgment

References

[1] K. Tüber, D. Pócza, C. Hebling, J. Power Sources 124 (2003) 403–414.
[2] X.G. Yang, F.Y. Zhang, A.L. Lubawy, C.Y. Wang, Electrochem. Solid-state Lett. 7 (2004) A408–A411.
[3] K. Sugiura, M. Nakata, T. Yodo, Y. Nishiguchi, M. Yamauchi, Y. Itoh, J. Power Sources 145 (2005) 526–533.
[4] K. Sugiura, T. Shiramizu, T. Yamauchi, M. Yamauchi, S. Matsuzaki, N. Kada, Y. Itoh, ECS Trans. 12 (2008) 131–138.
[5] K. Takada, Y. Ishigami, J. Inukai, Y. Nagumo, H. Takano, H. Nishide, M. Watanabe, J. Power Sources 196 (2011) 2635–2639.
[6] K. Takada, Y. Ishigami, S. Hirakata, M. Uchida, J. Inukai, H. Nishide, M. Watanabe, Electrochemistry 79 (2011) 388–391.
[7] M.A. Hickner, N.P. Siegel, K.S. Chen, D.N. McBrayer, D.S. Hussey, D.L. Jacobson, M. Arif, J. Electrochem. Soc. 153 (2006) A902–A908.
[8] Y.-S. Chen, H. Peng, D.S. Hussey, D.L. Jacobson, D.T. Tran, T. Abdel-Baset, M. Biernacki, J. Power Sources 170 (2007) 376–386.
[9] A. Turhan, K. Heller, J.S. Brenizer, M.M. Mench, J. Power Sources 180 (2008) 773–783.
[10] A.Z. Weber, M.A. Hickner, Electrochim. Acta 53 (2008) 7668–7674.
[11] M.A. Hickner, N.P. Siegel, K.S. Chen, D.S. Hussey, D.L. Jacobson, M. Arif, J. Electrochem. Soc. 155 (2008) B294–B302.
[12] M.A. Hickner, N.P. Siegel, K.S. Chen, D.S. Hussey, D.L. Jacobson, M. Arif, J. Electrochem. Soc. 155 (2008) B427–B434.
[13] H. Murakawa, T. Ueda, T. Yoshida, K. Sugimoto, H. Asano, N. Takenaka, K. Mochiki, H. Iikura, R. Yasuda, M. Matsubayashi, Nucl. Instr. Meth. A 605 (2009) 127–130.
[14] M.A. Hickner, N.P. Siegel, K.S. Chen, D.S. Hussey, D.L. Jacobson, J. Electrochem. Soc. 157 (2010) B32–B38.
[15] P.K. Sinha, P.P. Mukherjee, C.-Y. Wang, J. Mater. Chem. 17 (2007) 3089–3103.
[16] S.J. Lee, N.-Y. Lim, S. Kim, G.-G. Park, C.-S. Kim, J. Power Sources 185 (2008) 867–870.
[17] F.-Y. Zhang, S.G. Advani, A.K. Prasad, M.E. Boggs, S.P. Sullivan, T.P. Beebe Jr., Electrochim. Acta 54 (2009) 4025–4030.
[18] T. Sasabe, S. Tsushima, S. Hirai, K. Minami, K. Yada, ECS Trans. 25 (2009) 513–521.
[19] S. Tsushima, K. Teranishi, S. Hirai, Electrochem. Solid-state Lett. 7 (2004) A269–A272.
[20] S. Tsushima, T. Nanjo, S. Hirai, ECS Trans. 11 (2007) 435–443.
[21] K.W. Feindel, S.H. Bergens, R.E. Wasylishen, J. Power Sources 173 (2007) 86–95.
[22] J. Inukai, K. Miyatake, K. Takada, M. Watanabe, T. Hyakutake, H. Nishide, Y. Nagumo, M. Watanabe, M. Aoki, H. Takano, Angew. Chem. Int. Ed. 47 (2008) 2792–2795.
[23] T. Hyakutake, Y. Ishigami, J. Kato, J. Inukai, K. Miyatake, H. Nishide, M. Watanabe, Macromol. Chem. Phys. 212 (2011) 42–47.
[24] Y. Ishigami, K. Takada, H. Yano, J. Inukai, M. Uchida, Y. Nagumo, T. Hyakutake, H. Nishide, M. Watanabe, J. Power Sources 196 (2011) 3003–3008.
[25] J. Inukai, K. Miyatake, Y. Ishigami, M. Watanabe, T. Hyakutake, H. Nishide, Y. Nagumo, M. Watanabe, A. Tanaka, Chem. Commun. (2008) 1750–1752.
[26] T. Hyakutake, H. Taguchi, J. Kato, H. Nishide, M. Watanabe, Macromol. Chem. Phys. 210 (2009) 1230–1234.
[27] W. Waskitoaji, T. Hyakutake, J. Kato, M. Watanabe, H. Nishide, Chem. Lett. 38 (2009) 1164–1165.
[28] W. Waskitoaji, T. Hyakutake, M. Watanabe, H. Nishide, React. Funct. Polym. 70 (2010) 669–673.
[29] M. Yoneda, M. Takimoto, in: Proceedings of the ASME 8th International Conference on Fuel Cell Science, Engineering, and Technology, vol. 1, 2010, pp. 497–504.
[30] Y. Hashimasa, T. Numata, K. Moriya, S. Watanabe, J. Power Sources 155 (2006) 182–189.
[31] Y. Ishigami, I. Maeda, K. Takada, T. Hyakutake, T. Suga, J. Inukai, M. Uchida, Y. Nagumo, H. Nishide, M. Watanabe, Electrochem. Solid-state Lett. 15 (2012) B51–B53.
[32] C.Y. Wang, Chem. Rev. 104 (2004) 4727–4766.
[33] T.V. Nguyen, R.E. White, J. Electrochem. Soc. 140 (1993) 2178–2185.
[34] T.E. Springer, T.A. Zawodzinski, S. Gottesfeld, J. Electrochem. Soc. 138 (1991) 2334–2342.
[35] M. Hara, J. Inukai, K. Miyatake, H. Uchida, M. Watanabe, Electrochim. Acta 58 (2011) 449–455.
[36] M. Hara, J. Inukai, B. Bae, T. Hoshi, K. Miyatake, M. Uchida, H. Uchida, M. Watanabe, Electrochim. Acta 82 (2012) 277–283.

List of Symbols

i: local current density [A m^{-2}]
i_0: exchange current density [A m^{-2}]
θ: rate of catalyst utilization [−]
G: energy of activation [J kg^{-1}]
F: Faraday constant [C mol^{-1}]
R: gas constant [J mol^{-1} K^{-1}]
α_a: electrochemical kinetic rate [−]
η_a: activation over-potential [V]
η_r: Ohmic over-potential in electrolyte membrane [V]
T: temperature [K]
ρ: density [kg m^{-3}]
h: enthalpy [J kg^{-1}]
$\mathbf{u}$: velocity [m s^{-1}]
p: pressure [Pa]
s: water saturation [−]
p_c: capillary pressure in porous media [Pa]
a_v: water vapor activity [−]
K: permeability [m^{-2}]
μ: viscosity [Pa s]
ε: porosity of porous media [−]
w: molecular weight [kg mol^{-1}]
c: molecular concentration [mol m^{-3}]
D: gas diffusivity [m^2 s^{-1}]
κ: thermal conductivity [W m^{-1} K^{-1}]
$\dot{m}_p$: mass production rate by electrochemical reaction [kg m^{-3} s^{-1}]
$\dot{m}_{gl}$: mass production rate by phase change [kg m^{-3}s^{-1}]
ω_{gl}: phase change rate [s^{-1}]
d_e: equivalent hydraulic diameter of gas-flow channel [m]
n_d: osmotic drag coefficient [−]
D_w: water diffusivity [m^2 s^{-1}]
EW: equivalent weight [kg mol^{-1}]
λ: water content [−]

Superscripts

ref: reference properties
eff: effective properties
k: gas component

Subscripts

(k): =(a) anode side/*=(c)* cathode side in the catalyst layer
(m): polymer electrolyte membrane
g: gas phase
l: liquid phase
s: solid phase